Title

Sensor Reduction, Estimation, and Control of an Upper-Limb Exoskeleton

Journal

IEEE Robotics and Automation Letters, 6(2)

ISSN

2377-3766 2377-3774

Authors

Sun, Jianwei
Shen, Yang
Rosen, Jacob

Publication Date

2021-02-02

DOI

10.1109/LRA.2021.3056366

Peer reviewed

Sensor Reduction, Estimation, and Control of an Upper-Limb Exoskeleton

Jianwei Sun[1], Yang Shen[1], and Jacob Rosen[1]

***Abstract*—A multi-degree-of-freedom (multi-DOF) exoskeleton relies on an array of sensors to communicate its state (e.g., positions/orientations) and operator-exoskeleton contact interactions (e.g., forces/torques) to its control system. Although sensor redundancy is common in biological systems to cope with uncertainty and partial failure of sensors, in man-made systems, sensor redundancy increases the overall system's cost and control complexity. This study presents a sensor reduction technique for force/torque (F/T) sensors utilizing a Kalman filter-based sensor fusion system in the context of admittance control. The methodology is applied to the EXO-UL8 exoskeleton, which is a powered, redundant, dual-arm, upper-limb robotic system with (7 arm + 1 hand) DOFs incorporating three 6-axis F/T sensors in each arm. Motivated by improving wearability through minimizing human-exoskeleton contact interfaces, which reduces spurious contact forces due to joint misalignment; and reducing cost, the proposed strategy emulates the admittance controller's virtual dynamics with only a subset of sensors, resulting in the physical human-robot interaction feeling the same from the operator's perspective. Experimental results indicate that human-exoskeleton power exchange and actuation stresses of the operator's joints, with the proposed strategy on a subset of two sensors, are comparable to those in the full three-sensor case ($p < 0.01$). The experiments verify the proposed methodology for the EXO-UL8, and support the feasibility of operating other Kalman filter-based sensor fusion systems with fewer sensors without sacrificing transparency in physical human-robot interaction.**

***Index Terms*—Compliance and Impedance Control, Physical Human-Robot Interaction, Prosthetics and Exoskeletons, Wearable Robotics, Rehabilitation Robotics.**

I. Introduction

In this paper, a method of sensor reduction is presented for a force estimation sensor fusion algorithm in the context of admittance control for the EXO-UL8 exoskeleton [1]–[3].

Force sensing and estimation are prevalent in the field of exoskeleton [4]–[9] and robotics control [10]–[16]. Force sensing includes resolving sensor redundancies and finding optimal sensor placement [8], [10]–[12], whereas force estimation includes sensorless approaches, such as using disturbance observers [5], [8] or other model-based state estimators/filters [4], [9], [14]–[16]. These techniques have found applications in teleoperation [15], [16], exoskeleton control [4]–[9], human-robot interaction [13], and other applications in which the use of sensors is limited by feasibility, reliability, or cost.

Manuscript received: August, 26, 2020; Revised: November, 16, 2020; Accepted: January, 13, 2021.

This paper was recommended for publication by Editor Pietro Valdastri upon evaluation of the Associate Editor and Reviewers' comments.

[1]The authors are with the Department of Mechanical and Aerospace Engineering, Bionics Lab, University of California, Los Angeles, CA, 90095 USA. {sunjianw1,yangshen,jacobrosen}@ucla.edu

Digital Object Identifier (DOI): see top of this page.

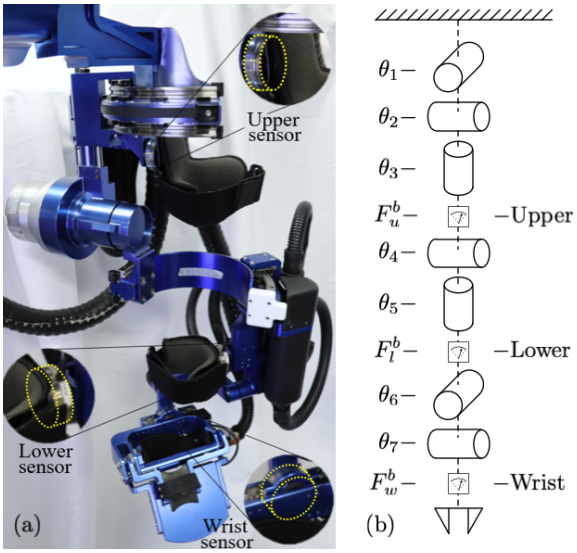

Fig. 1. (a) On each arm (right arm shown), the upper and lower force/torque sensors interface with an operator's arm via elastic cuff links. The wrist sensor is embedded into the gripper. (b) Each arm can be analyzed as a serial manipulator with joints corresponding to those of a human arm: $\{\theta_1, \theta_2\}$ - shoulder abduction/adduction and flexion/extension, θ_3 - shoulder interior/exterior rotation, θ_4 - elbow flexion/extension, θ_5 - forearm pronation/supination, θ_6 - wrist extension/flexion, and θ_7 - wrist radial/ulnar deviation.

Sensorless force estimation, such as in the flying probe of [14], the exoskeletons of [4], [5], and the quadrocopter of [13], estimate external contact forces through knowledge of the system dynamics. Unlike the exoskeletons of [5], [8], [9], the EXO-UL8 does not have back-driveable joints in order to achieve higher joint payload capacity. As a result, sensorless approaches could not be utilized.

Applications in which the use of sensors is limited have necessitated the exploration of sensor reduction techniques. These include sensorless approaches, as described above, or reducing the number of required sensors, which is the focus of this research. In the latter case, existing literature has formulated the problem of selecting an optimal subset of sensors as minimizing some cost function [10]–[12]. While these approaches typically deal with a large number of sensors and are concerned with the optimal subset of sensors, our paper aims to show that different subsets of sensors can be tuned to yield similar dynamic responses as the full set.

In resolving sensor redundancy, literature has explored sensor fusion techniques such as Kalman filtering [17]–[19], fuzzy logic approaches [18], [20], Monte Carlo methods [21], and other weighted sum approaches [2], [8]. Whereas the ARMIN IV+ of [8] uses a constant weighted sum to combine sensor

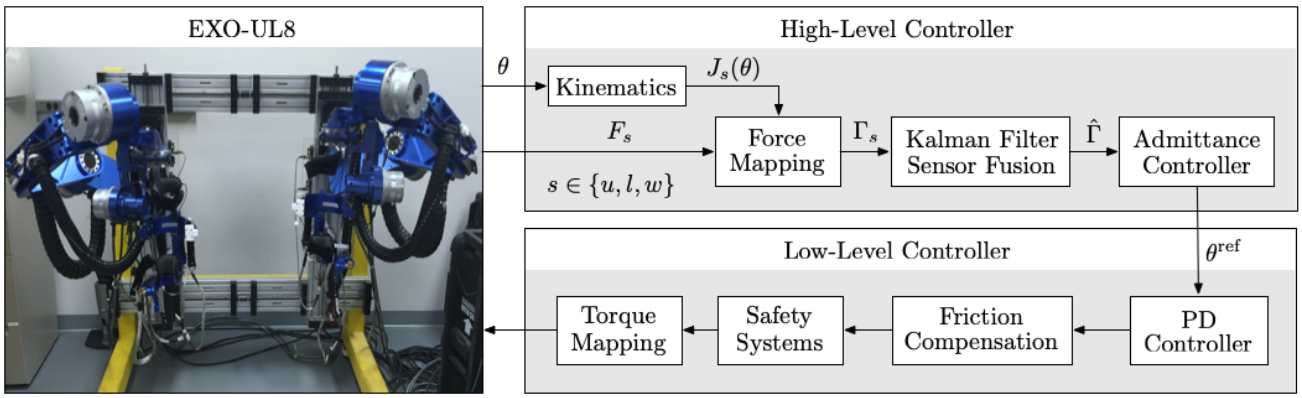

Fig. 2. The cascaded control scheme of the EXO-UL8 operates at 1kHz and consists of a high-level controller, which contains the Kalman filter-based sensor fusion block and admittance controller, and a low-level controller, which tracks joint-space reference trajectories. Relevant signals are labeled.

inputs, our approach uses a Kalman filter to account for state-dependency of the sensor fusion gains, as the arm's ability to generate force is position-dependent [3].

Many variations of Kalman filtering are utilized in robotic state estimation and control. [22] implements the Extended Kalman filter to estimate joint angles from the nonlinear dynamics of muscle tension control in a redundant musculoskeletal humanoid. [14] implements a modified Kalman filter with acceleration estimation for a flying probe system. In [23], the authors utilize the Unscented Kalman filter in pose estimation to enable backstepping control of a mobile robot. In our work, we utilize the linear Kalman filter for sensor fusion.

The EXO-UL8 is a dual-arm, powered, redundant, upper-limb exoskeleton with seven active *degrees-of-freedom* (DOF) and one active gripper DOF on each arm [1]–[3] designed to support research efforts in robot-assisted rehabilitation. The exoskeleton tracks an operator's movements through admittance control in joint-space. The admittance controller is driven by operator-applied forces that are measured by three 6-axis force/torque sensors (ATI Mini40) located at the upper arm, lower arm, and wrist, as shown in Fig. 1. Reducing the number of required sensors in the EXO-UL8 is motivated by:

1) Improved wearability: During donning, a patient's arm must pass through each of the elastic cuffs, akin to putting one's arm through the sleeve of a sleeved shirt. For patients with neuromuscular disorders such as coupled joint movements or muscular spasticity, such a maneuver is difficult or impossible.
2) Joint alignment: Misalignment of the rotational axes of the EXO-UL8's joints with those of anatomical joints can result in large contact forces to the operator [24]. The absence of a sensor can provide increased scapular movement freedom so that the operator can actively correct for joint misalignment.
3) Reduced cost: If fewer sensors can achieve similar performance, then component cost can be lowered.

While existing literature explores optimal sensor placement, sensor fusion, and sensorless force-estimation and control, the main contribution of our paper is a Kalman filter tuning method to emulate the baseline admittance controller virtual dynamics (based on the full three-sensor case) with only two of the three sensors, resulting in the interaction feeling the same from the operator's perspective.

The rest of the paper is organized as follows: section II describes the filtering and control strategies of the EXO-UL8, section III examines the minimum required number of sensors and the compensation for a missing sensor, and section IV describes the experimental validation of the proposed method.

II. System Architecture

A. Cascaded Control Scheme

The EXO-UL8 implements a cascaded control scheme in which the sensor fusion block combines measured forces into a torque signal. The torques are then input to the admittance controller, which generates joint-space trajectories tracked by *proportional-derivative* (PD) motor joint controllers. Fig. 2 shows a block diagram of the control architecture.

B. Sensor Torque Mapping and Fusion

The EXO-UL8 was originally designed with three 6-axis force/torque sensors on each of its two arms: one at the upper arm (u), one at the lower arm (l), and one integrated into the wrist assembly (w), as shown in Fig. 1. Each sensor $s \in \{u, l, w\}$ provides a wrench measurement, $F_s^b \in \mathbb{R}^6$, in its body reference frame, as indicated by the b superscript. To enable compatible operations, each measured wrench F_s^b is transformed to the spatial frame, located at the intersection of the three shoulder axes of rotation, through:

$$F_s^{sp} = \mathrm{Ad}_{g_s^{-1}(\theta)}^{\top} F_s^b, \tag{1}$$

where $F_s^{sp} \in \mathbb{R}^6$ expresses the equivalent wrench in the spatial frame, and $\mathrm{Ad}_{g_s} \in \mathbb{R}^{6\times 6}$ is the corresponding adjoint matrix for the homogeneous transformation $g_s \in \mathrm{SE}(3)$ from the spatial frame to the sensor's body frame. The transformed wrenches, F_s^{sp}, are then mapped to joint torques $\Gamma_s \in \mathbb{R}^7$ with the spatial manipulator Jacobian:

$$\Gamma_s = J_s(\theta)^{\top} F_s^{sp}. \tag{2}$$

Note that $J_u(\theta) \neq J_l(\theta) \neq J_w(\theta)$ because the dimensions are different due to each sensor being located at a different position along the kinematic chain, as shown in Fig. 1.

The torque contributions from the sensors are then combined via a *linear time-invariant* (LTI) sensor fusion system to yield joint torques $\hat{\Gamma} \in \mathbb{R}^7$ to input to the admittance controller. The sensor fusion system is represented as:

$$\begin{aligned} x_\Gamma[k+1] &= A_\Gamma x_\Gamma[k] + B_\Gamma \operatorname{col}(\Gamma_u[k], \Gamma_l[k], \Gamma_w[k]), \\ \hat{\Gamma}[k] &= C_\Gamma x_\Gamma[k] + D_\Gamma \operatorname{col}(\Gamma_u[k], \Gamma_l[k], \Gamma_w[k]), \end{aligned} \tag{3}$$

where $x_\Gamma[k] \in \mathbb{R}^{n_\Gamma}$ is the state of the sensor fusion at time step k, $(A_\Gamma, B_\Gamma, C_\Gamma, D_\Gamma)$ are state-space matrices in minimal realization, and $\operatorname{col}(\cdot, \ldots, \cdot)$ produces a column vector from its arguments. The sensor fusion system is expressed in discrete-time to support software implementation.

C. Sensor Fusion via Kalman Filtering

A Kalman filter-based sensor fusion combines the torques from the sensors $(\Gamma_u, \Gamma_l, \Gamma_w)$ into a single torque estimate $\hat{\Gamma}$. Since the joint torques are generated from human-applied forces, the exact signal is not known a priori. Therefore, the process equation for Γ is modeled as a random walk, similar to the technique used in [1], [13]:

$$\Gamma[k+1] = \Gamma[k] + (\Delta t) w_\Gamma[k], \tag{4}$$

where Δt is the sampling period, and $w_\Gamma[k] \sim \mathcal{N}(0, Q_\Gamma)$, where Q_Γ is an empirically tuned covariance matrix. The torques $\Gamma_u, \Gamma_l, \Gamma_w$ are then treated as measurements with additive Gaussian noise to the Kalman filter:

$$z[k] := \begin{bmatrix} \Gamma_u[k] \\ \Gamma_l[k] \\ \Gamma_w[k] \end{bmatrix} + \begin{bmatrix} w_u[k] \\ w_l[k] \\ w_w[k] \end{bmatrix}, \tag{5}$$

$$= \begin{bmatrix} \mathbb{I}_{3\times3} & \mathbb{0}_{3\times4} \\ \mathbb{I}_{5\times5} & \mathbb{0}_{5\times2} \\ & \mathbb{I}_{7\times7} \end{bmatrix} \Gamma[k] + \begin{bmatrix} w_u[k] \\ w_l[k] \\ w_w[k] \end{bmatrix}, \tag{6}$$

$$:= H\Gamma[k] + \operatorname{col}(w_u[k], w_l[k], w_w[k]), \tag{7}$$

where $z[k] \in \mathbb{R}^{15}$ is a combined vector of joint torques from the sensors. $w_u[k] \sim \mathcal{N}(\mathbb{0}_{3\times1}, R_u)$, $w_l[k] \sim \mathcal{N}(\mathbb{0}_{5\times1}, R_l)$, and $w_w[k] \sim \mathcal{N}(\mathbb{0}_{7\times1}, R_w)$, where $R_u \in \mathbb{R}^{3\times3}$, $R_l \in \mathbb{R}^{5\times5}$, and $R_w \in \mathbb{R}^{7\times7}$ are the noise covariance matrices corresponding to the upper, lower, and wrist sensor, respectively. Let $\hat{\Gamma} \in \mathbb{R}^7$ be the *minimum mean squared error* (MMSE) estimate of Γ, $P_p \in \mathbb{R}^{7\times7}$ be the variance of the a priori, $P_m \in \mathbb{R}^{7\times7}$ be the variance of the a posteriori, and $R := \operatorname{diag}(R_u, R_l, R_w)$. Then, the update equations for the Kalman filter become:

Initialization:

$$\hat{\Gamma}[0] = \mathbb{0}_{7\times1}, \tag{8}$$

$$P_m[0] = (\Delta t)^2 Q_\Gamma. \tag{9}$$

A Priori Update:

$$P_p[k] = P_m[k-1] + (\Delta t)^2 Q_\Gamma. \tag{10}$$

A Posteriori Update:

$$K[k] := P_p[k] H^\top (H P_p[k] H^\top + R)^{-1}, \tag{11}$$

$$\hat{\Gamma}[k] = (\mathbb{I} - K[k]H)\hat{\Gamma}[k-1] + K[k] z[k], \tag{12}$$

$$\begin{aligned} P_m[k] = (\mathbb{I} - K[k]H) P_p[k] (\mathbb{I} - K[k]H)^\top \\ + K[k] R K[k]^\top, \end{aligned} \tag{13}$$

where $K[k] \in \mathbb{R}^{7\times15}$ is defined as the Kalman gain at time step k. Note that equation (13) implements the Joseph form for numerical stability.

The Kalman filter implemented in this form is not time-invariant, so it cannot be expressed in the form of equation (3). However, this is not problematic because convergence of the Kalman filter is guaranteed by $(\mathbb{I}_{7\times7}, H)$ being detectable and $(\mathbb{I}_{7\times7}, Q_\Gamma^{1/2})$ being stabilizable [25], where $\mathbb{I}_{7\times7}$ is the state transition matrix in equation (4). Then, let P_∞ be the steady-state a posteriori variance calculated from the discrete algebraic Riccati equation and let $K_\infty = P_\infty H^\top (H P_\infty H^\top + R)^{-1}$ be the steady-state Kalman gain [19]. The updated equations become:

$$\hat{\Gamma}[k] = (\mathbb{I} - K_\infty H)\hat{\Gamma}[k-1] + K_\infty z[k], \tag{14}$$

which is a discrete-time, linear time-invariant system.

III. Sensor Reduction

A. Admittance Controller

The estimated joint torques, $\hat{\Gamma}$, from the sensor fusion system are then used to drive a first-order reference-generation model in joint-space:

$$\tau_j \dot{\theta}_j^{\text{ref}} + \theta_j^{\text{ref}} = a_j \hat{\Gamma}_j, \ j \in \{1, \ldots, 7\}, \tag{15}$$

where $\tau_j, a_j \in \mathbb{R}$, $\tau_j > 0$, $a_j > 0$ are the time constant and DC gain of the model for joint j, and $\theta^{\text{ref}} \in \mathbb{R}^7$ is the generated reference signal to be tracked by the motor controllers. These constants are experimentally tuned to achieve responsive behavior of the EXO-UL8, as qualitatively determined by test users. In the Laplace domain, each channel of equation (15) has a pole at $s = -\tau_j^{-1}$, which is stable since $\tau_j > 0$. Furthermore, the model can be exactly discretized to:

$$\theta_j^{\text{ref}}[k+1] = e^{-\frac{\Delta t}{\tau_j}} \theta_j^{\text{ref}}[k] + a_j (1 - e^{-\frac{\Delta t}{\tau_j}}) \hat{\Gamma}_j[k], \tag{16}$$

for each joint, $j \in \{1, \ldots, 7\}$. The discretized model ensures that discretization errors are minimal.

A summary of the control scheme implementation is given in Procedure 1. The procedure is implemented as an interrupt handler for a timer with interrupt frequency of 1kHz.

Procedure 1: 1kHz Timer Interrupt Handler

```
θ ← Read joint angles
for s ∈ {u, l, w} do
    F_s^b ← Read force sensor
    F_s^sp ← Ad^⊤_{g_s^{-1}(θ)} F_s^b                ▷ Eqn (1)
    Γ_s ← J_s(θ)^⊤ F_s^sp                            ▷ Eqn (2)
KF a priori update                                   ▷ Eqn (10)
Γ̂ ← KF a posteriori update                           ▷ Eqns (11)-(13)
for j ∈ {1, ..., 7} do
    θ_j^ref ← Update virtual dynamics                ▷ Eqn (16)
Send θ^ref to Low-Level Controller
```

B. Minimum Number of Sensors

In non-singular configurations of the joint angles, the wrist Jacobian, $J_w(\theta)$, is the only Jacobian that can affect all seven dimensions of the joint torque vector, $\hat{\Gamma}$. For this reason, it must be included in the control strategy. Additionally, at least one of the upper or lower sensors must also be present. To illustrate this requirement, consider the case in which only the wrist sensor provides the joint torques used by the admittance controller:

$$\hat{\Gamma} = \Gamma_w = J_w(\theta)^\top F_w. \tag{17}$$

In order for the single sensor to provide enough information to fully control the exoskeleton, the map between the space of wrenches ($\mathbb{R}^6$) to the space of joint torques ($\mathbb{R}^7$) must be surjective. Due to the limited dimensionality of the space of wrenches, there does not exist a mapping that satisfies this requirement. In fact, the wrench can only map to a six-dimensional subspace in $\mathbb{R}^7$, assuming that the Jacobian does not lose rank from the exoskeleton being in a singular configuration. The orthogonal complement of the column space of $J_w(\theta)^\top$ is the left nullspace of $J_w(\theta)^\top$, or simply the nullspace of $J_w(\theta)$. Since $J_w(\theta) \in \mathbb{R}^{6\times7}$ and has full row rank, the dimension of its nullspace is one, and corresponds to the manifold of internal motions on which $J_w(\theta)\dot{\theta} = 0$. This manifold contains the motions along the swivel angle in which the wrist maintains its position in end-effector space while the elbow is free to rotate [3], [26]. The redundancy of the EXO-UL8 means that the wrist sensor alone cannot provide enough information, so at least one other sensor must also be present. Thus, a total of two sensors are utilized.

C. Feasibility of Two Sensors

When two of the 6-axis force/torque sensors are included, a total of twelve inputs are provided to the exoskeleton to actuate seven joints. The Kalman filter in the admittance control scheme serves as a sensor fusion system whose outputs are estimates of the joint torques. Feasibility of requiring only two sensors is equivalent to controllability of the Kalman filter when interpreted as an LTI system. Therefore, if the sensor fusion system described by equation (14) is controllable, there exist inputs from the sensors that can drive the torque estimate to any point in the state-space. The pair $(K_\infty, \mathbb{I} - K_\infty H)$ is controllable if and only if its controllabilty matrix is full rank:

$$\mathcal{C} = [K_\infty \quad (\mathbb{I} - K_\infty H)K_\infty \quad \dots \quad (\mathbb{I} - K_\infty H)^6 K_\infty]. \tag{18}$$

Since the Kalman filter converges, as shown in subsection II-C, the steady-state Kalman gain, $K_\infty \in \mathbb{R}^{7\times15}$ is necessarily full rank. The first block column of $\mathcal{C}$ is K_∞, so the controllability matrix must already have a column rank of 7. Therefore, the sensor fusion system is controllable and the inputs from the two sensors are sufficient to produce any joint torque estimate.

D. Sensor Fusion Tuning to Compensate for Fewer Sensors

The absence of an upper or lower sensor impacts the interaction dynamics experienced by the operator; more force may be required to move the exoskeleton in certain directions. To ensure that the interaction feels the same from the operator's perspective when only two of the three sensors are utilized, the baseline (full three-sensor case) admittance controller virtual dynamics must be emulated. This is achieved by tuning the Kalman filter in either of the reduced-sensor cases to have the same filter dynamics as in the baseline. In both cases, the admittance controller receives the same input and generates the same virtual dynamics. The details of this tuning strategy are explained in this section.

Let the sensor configurations be denoted as:

(A) All three sensors (upper, lower, wrist),
(B) Lower and wrist sensors only,
(C) Upper and wrist sensors only.

From equation (15), the same joint trajectories are generated if the $\hat{\Gamma}$ output from the Kalman filter remains the same. Equation (14) shows that the steady-state Kalman gain, K_∞, and the measurement matrix, H, directly affect the filter dynamics. For the subsequent analysis, let:

$$H_{lw} := \begin{bmatrix} \mathbb{I}_{5\times5} & \mathbb{0}_{5\times2} \\ & \mathbb{I}_{7\times7} \end{bmatrix}, \tag{19}$$

which denotes the measurement matrix used to define $z_{lw}[k]$ in the Kalman filter a posteriori update equations, and corresponds to the case in which the upper sensor is absent (config. B). Then, to ensure that equation (14) remains the same in configurations A and B, it is required that:

$$K_\infty H = \tilde{K}_\infty H_{lw}, \tag{20}$$

where $\tilde{K}_\infty$ denotes the modified steady-state Kalman gain. Expanding equation (20), the requirement becomes:

$$\begin{aligned} &H^\top \left(H P_\infty H^\top + R\right)^{-1} H \\ &= H_{lw}^\top \left(H_{lw} P_\infty H_{lw}^\top + R_{lw}\right)^{-1} H_{lw} \end{aligned} \tag{21}$$

where $R_{lw} \in \mathbb{R}^{12\times12}$ is the new diagonal measurement covariance to be determined. Note that the estimation error covariance, P_∞, should be the same in both cases to ensure that the removal of one sensor does not change the steady-state performance of the Kalman filter. Then, the objective is to solve equation (21) for the only unknown, R_{lw}.

Note that the matrices H and H_{lw} are related by:

$$H = \begin{bmatrix} \mathbb{I}_{3\times3} & \mathbb{0}_{3\times9} \\ & \mathbb{I}_{12\times12} \end{bmatrix} H_{lw} := E H_{lw}. \tag{22}$$

Finding an appropriate matrix E is always possible when H_{lw} has full row rank, which is a necessary requirement for the Kalman filter to converge in this case. Then, the left side of equation (21) becomes:

$$= H_{lw}^\top E^\top \left(H P_\infty H^\top + R\right)^{-1} E H_{lw}. \tag{23}$$

By equating the matrices between the $H_{lw}^\top$ and H_{lw} terms, R_{lw} is solved as:

$$R_{lw} = \left[E^\top \left(H P_\infty H^\top + R\right)^{-1} E\right]^{-1} - H_{lw} P_\infty H_{lw}^\top. \tag{24}$$

A similar analysis calculates $R_{uw} \in \mathbb{R}^{10\times10}$ for configuration C. Equation (24) computes the necessary measurement noise covariance matrix to achieve equal filter dynamics to the nominal case, despite the absence of a sensor.

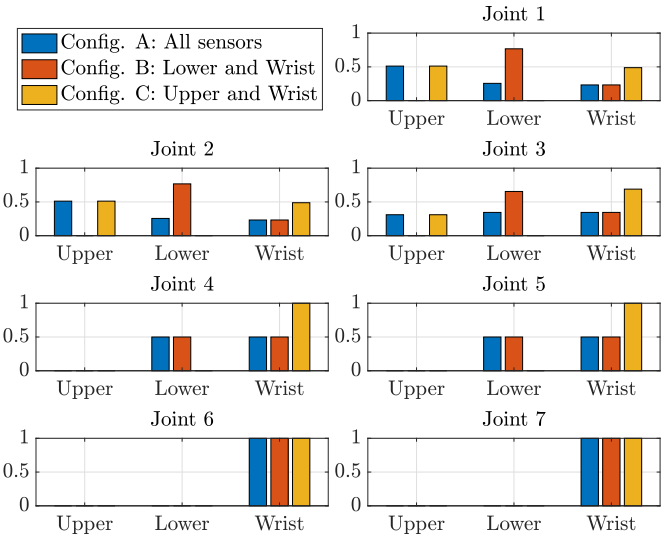

Fig. 3. The theoretical normalized sensor contributions to the estimated torque are determined by normalizing the reciprocal of the variance values for each sensor with the sum of the reciprocal variance values in each sensor configuration. Joints located farther down the kinematic chain are affected by fewer sensors, as in the case of Joints $4-7$. In all cases, the removal of a sensor redistributes the relative contributions of the remaining sensors.

When the Kalman filter reaches steady state, the contribution of each measurement to the estimate is proportional to the inverse of the associated noise variance. Thus, to visualize how sensor contributions change, it suffices to consider how the noise variances in R_{lw} (config. B) and R_{uw} (config. C) differ from those in R_u, R_l, R_w (config. A). For example, the contribution of the lower sensor to joint 1 in config. A is:

$$\frac{1/R_l(1,1)}{1/R_u(1,1)+1/R_l(1,1)+1/R_w(1,1)} \approx 0.256. \tag{25}$$

However, when the upper sensor is removed (config. B), the contribution of the lower sensor becomes:

$$\frac{1/R_{lw}(1,1)}{1/R_{lw}(1,1)+1/R_{lw}(6,6)} \approx 0.767. \tag{26}$$

The increase indicates that when the upper sensor is removed, the Kalman filter places greater emphasis on the measurement of the lower sensor in order to yield the same dynamics. Fig. 3 summarizes the distributions of sensor contributions in each of the three configurations.

IV. Experiments

All experiments in this study were performed with a healthy right-handed participant (male, 25-years-old) following an approved Institutional Review Board protocol (IRB #18-00766).

A. Performance Metrics

1) NASA Task Load Index (NASA-TLX): The term *transparency* is a measure of the exoskeleton's tracking performance to an operator's movements. Although it can be quantified using the metrics defined below, a qualitative assessment of ease of control and wearability, as provided by the operator, is also an important indication of performance. To this end, the NASA-TLX survey [27] was utilized to assess the quality of the interaction and ease of donning for each of the three sensor configurations.

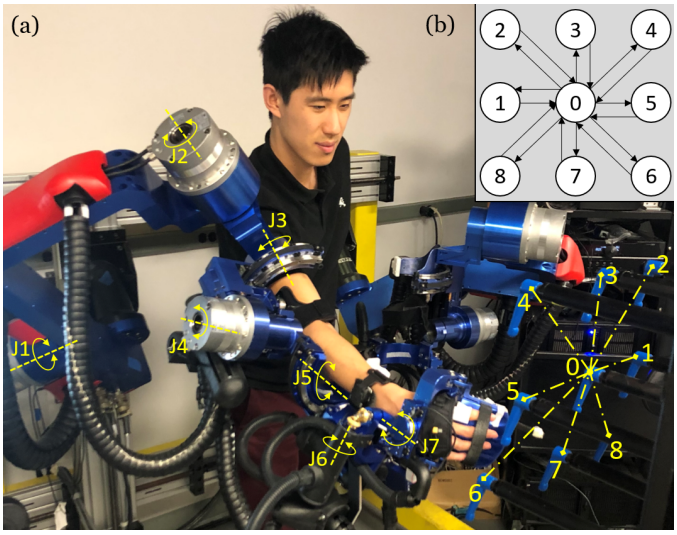

Fig. 4. (a) A subject wears the exoskeleton to accomplish the trajectory-following tasks; (b) Planned trajectory.

2) Power Exchange: In an ideal interaction, no force occurs at the physical human-exoskeleton interface (sensor locations). During motion, this is equivalent to zero mechanical power exchanged. Therefore, the power exchanged through the sensors can quantify the transparency of the interaction; the smaller the power exchanged, the more ideal the interaction. Let $v_s^{sp} \in \mathbb{R}^6$ be the linear and angular velocity of sensor s expressed in the spatial frame. Then the instantaneous power exchange for sensor s is the inner product between the wrench and velocity: $P_s(t) := \langle F_s^{sp}(t), v_s^{sp}(t) \rangle$. The mean power exchange over an interval $t \in [0, T]$ is then:

$$P_s^{\text{avg}} := \frac{1}{T}\int_0^T \langle F_s^{sp}(\tau), v_s^{sp}(\tau) \rangle \, \mathrm{d}\tau. \tag{27}$$

3) Actuation Stress: As another metric for transparency, the actuation stress is defined as a normalization of the effort contributed by each joint in the operator's arm during motion. The less torque each joint has to produce relative to its limit, the lower the actuation stress. Quantitatively, the actuation stress for joint $j \in \{1, \ldots, 7\}$ is defined as:

$$S_j(t) := \frac{|\hat{\Gamma}_j(t)|}{\Gamma_j^{\max}} \times 100\%, \tag{28}$$

where $\hat{\Gamma}_j(t)$ is the estimated torque from the Kalman filter, and $\Gamma_j^{\max}$ is the max joint torque that a human arm is able to exert. Table I shows typical anatomical values for $\Gamma_j^{\max}$ [28]. Note that the torque limits are direction-dependent due to differences in concentric and eccentric muscle contractions.

TABLE I
Direction-dependent joint torque limits

Joint	Positive Limit (Nm)	Negative Limit (Nm)
Shoulder	Flexion: 13.13 Adduction: 14.49 Internal Rotation: 11.59	Extension: 8.90 Abduction: 15.62 External Rotation: 11.63
Elbow	Flexion: 10.75	Extension: 8.76
Wrist	Pronation: 3.39 Extension: 2.11 Radial Deviation: 2.67	Supination: 1.42 Flexion: 1.55 Ulnar Deviation: 1.98

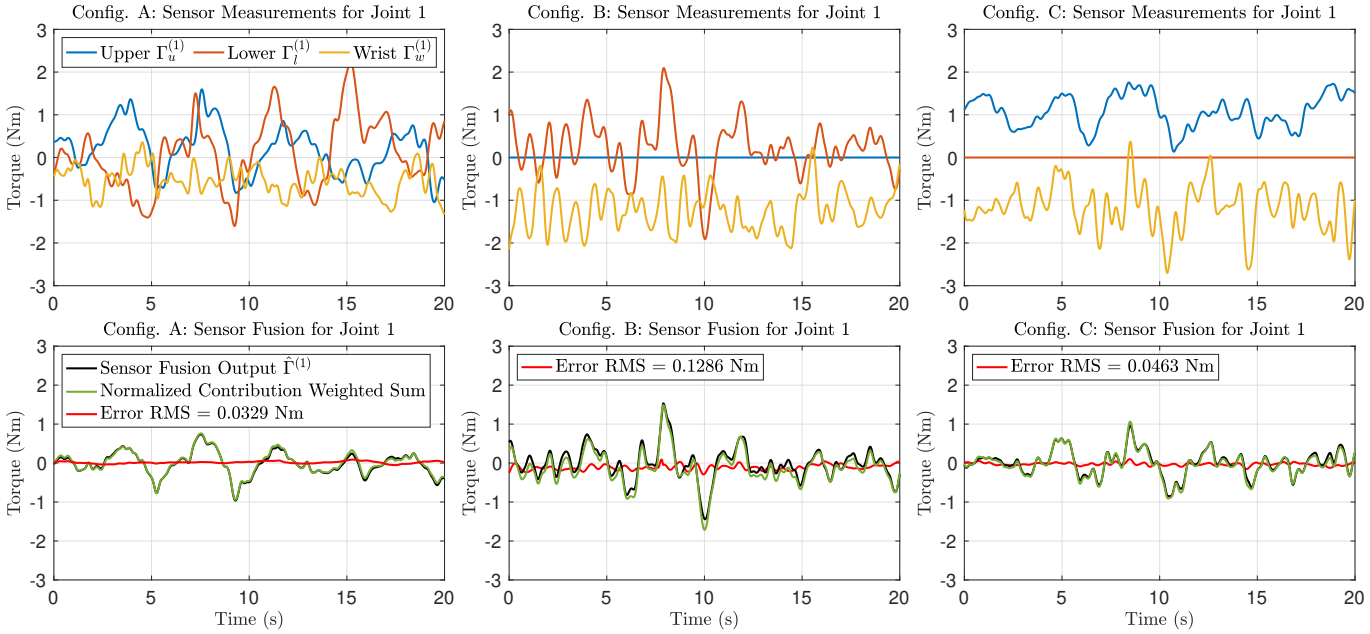

Fig. 5. A sample 20 second duration data fusion time-series is shown for joint 1 for the three sensor configuration cases. The three plots in the top row show the torque measurements Γ_s from equation (2) for the three sensors in the three configurations. The bottom row shows the corresponding sensor fusion outputs $\hat{\Gamma}$. The torque measurements are also combined in a weighted sum with the normalized contribution values from Fig. 3. The estimated torques output from the sensor fusion algorithm shows strong agreement with the expected results based on the compensated sensor noise covariance matrix in equation (24). The differences of the signals is also shown, and quantified by its RMS value. The small magnitudes of errors indicate that the analysis based on the steady-state Kalman filter in equation (14) is valid for the time-varying filter.

B. Experimental Setup

A reaching trajectory, as shown in Fig. 4, is used to assess the three sensor configurations. For configurations B and C, the attachment cuff for the unused sensor was also detached. As operator-exoskeleton force exchange occurs via the attachment cuffs, without a sensor to quantify the interaction forces, local dynamics may not be accurately captured, and may consequently harm transparency. Additionally, one of the primary motivators for removing sensors was to improve wearability by reducing the number of attachment cuffs that an operator's arm has to pass through to donn the exoskeleton.

The target trajectory in Cartesian space is designed to exercise a large range of motion. Physical markers (15 cm apart from each other) delineate the trajectory in front of the exoskeleton as shown in Fig. 4. The plane of the targets is located 75 cm in front of the operator, at a height at which the operator's outstretched arm is perpendicular to the operator's body when touching the topmost target. A 5 cm rubber pointer at the end-effector is used to make contact with the targets. To ensure comparable timescales across all experimental trials, the subject is given 2 seconds to complete each segment of the trajectory without stopping, for a total of 8×2 (forward and back) segments. A metronome with a 2 second period is used to pace the experiment. The subject also wears short-sleeved clothing to prevent inaccurate sensor readings caused by nonlinear deformation of clothing. Prior to each trial, the subject is given 3 minutes to become familiar with the operation of the exoskeleton. A total of 10 trials for each sensor configuration is carried out to ensure the statistical significance of results.

C. Results and Discussion

1) Qualitative Assessment: The NASA-TLX assessment for the three sensor configurations is shown in Table II. A lower number is favorable for all metrics except for Performance. The numbers in parentheses for configuration B and configuration C indicate the change from the corresponding task load in configuration A, which serves as the baseline. Qualitative assessment from the subject indicates little change in terms of exoskeleton operation and wearability, which is the desired result. However, configuration B indicates a slight increase in operational difficulty, likely due to more inaccuracies in estimating the torques of the shoulder joints as the closest sensor (upper) is removed in configuration B. This sensing limitation is also evident in the quantitative results described in the subsequent sections.

TABLE II
NASA-TLX ASSESSMENT FOR EACH SENSOR CONFIGURATION

Better	Scale (1 - 20)	Config. A	Config. B	Config. C
↓	Mental Demand	5	5	5
↓	Physical Demand	7	8 (+1)	6 (-1)
↓	Temporal Demand	10	11 (+1)	10
↑	Performance	5	6 (+1)	5
↓	Effort	7	8 (+1)	7
↓	Frustration	5	5	5

2) Sensor Contribution: Fig. 5 shows experimental data for the three sensor configurations for joint 1. The top row plots the joint torques converted from the sensor readings (equation (5)). The bottom row shows the output of the time-varying Kalman filter and a weighted sum of the torques from the first column using the theoretical contributions in Fig. 3. These

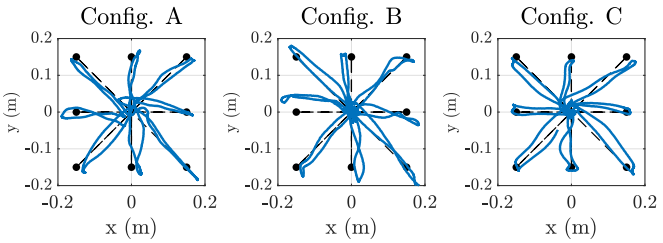

Fig. 6. End-effector trajectories in the plane of the target pattern for the three sensor configurations. Trajectories are overlayed onto the target pattern shown in Fig. 4. Each of the three configurations allows for satisfactory performance in enabling the operator to follow the target pattern.

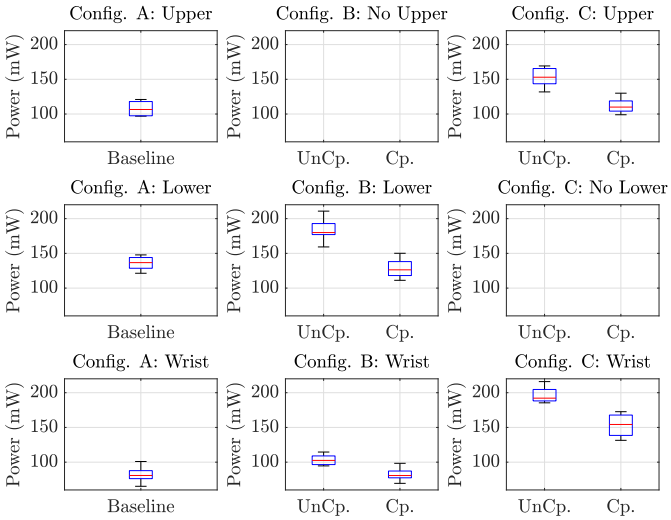

Fig. 7. The columns show the power exchange for configurations A, B, and C (left to right). Uncompensated (Uncp.) refers to the sensor configuration applied but without re-tuning the Kalman filter; i.e., the filter operates under the assumption that all sensors are present, even though a sensor is physically removed. On the other hand, compensated (Cp.) refers to tuning the filter's noise covariance matrices according to equation (24). Results indicate that after tuning, average power exchange decreases ($p < 0.01$), indicative of more transparent human-exoskeleton interaction.

were plotted together to show strong agreement, which indicates convergence of the Kalman filter. Demonstrating that the time-varying filter achieves expected results with experimental data validates the steady-state Kalman filter assumption used in calculating the theoretical sensor contributions of Fig. 3.

The bottom row of Fig. 5 also shows the error and its *root-mean-square* (RMS) to quantify the disagreement between the expected filter output and measured filter output. While configuration C shows agreement to the baseline (config. A) in terms of error RMS, configuration B shows a larger error, which agrees with the qualitative assessment. This may be caused by the removal of the closest sensor to joint 1 (upper sensor in configuration B). The lower and wrist sensors are located farther along the kinematic chain than the upper sensor, so their accurate estimation of the torque on joint 1, as compared to that of the upper sensor, is affected by a greater number of intermediate joints.

3) Power Exchange: Sample end-effector trajectories are shown in Fig. 6. Mean power exchange for the trials are computed with equation (27) and represented by the box-and-

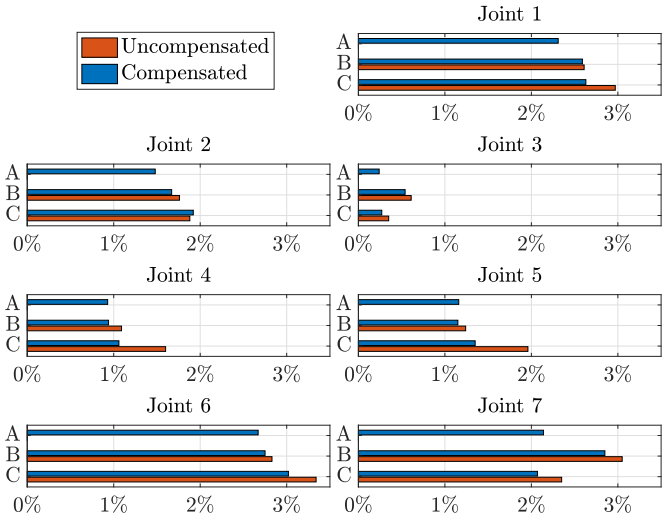

Fig. 8. Actuation stresses for the three sensor configurations show that compensation (re-tuning the Kalman filter) results in closer values to the baseline (config. A).

whisker plots in Fig. 7. Experimental results show that the compensated Kalman filters resulted in lower power exchange as compared to the uncompensated cases ($p < 0.01$). Statistical significance of the power exchange results was evaluated using the two-sample t-test. The null hypothesis for each sensor in configurations B and C was that the power exchange distributions of the compensated and uncompensated cases had equal mean but unknown variance. The alternative hypothesis was that the distributions had unequal means. In all four cases (B - lower, B - wrist, C - upper, C - wrist), the p-values were less than 0.01, with the largest being $p = 0.0089$ for the wrist sensor in configuration C, indicating that re-tuning the Kalman filter was statistically significant in improving transparency, when measured with the power exchange metric.

In configuration B, the mean power exchange of the compensated case closely matched that of the baseline, albeit with more variance. This is likely caused by the same limitation evident in the NASA-TLX qualitative assessment of Table. II and error RMS of Fig. 5: the removal of the upper sensor places more emphasis on the lower sensor to estimate torques for the shoulder joints (1-3), which may introduce additional uncertainties as there are now more intermediate joints between the shoulder and its closest sensor (lower).

In configuration C, the power exchange in the compensated case is higher than in the baseline. Since the lower and wrist sensors are only 12.5 cm apart, the absence of the lower sensor and its attachment cuff may cause the full mass of the operator's forearm to rest on only the wrist attachment, resulting in higher sensor readings. This anomaly is not present in configuration B (upper sensor absent) because the mass of the operator's upper arm is supported by their shoulder and does not rest on the upper sensor. With the upper sensor absent, the compensated cases match more closely with the baseline.

4) Actuation Stress: The actuation stresses are computed with equation (28), averaged across the trials, and shown in Fig. 8. Between the compensated and uncompensated cases, all joints except for joint 2 show a lower actuation stress when

the remaining sensors are re-tuned according to section III-D, which agrees with the power exchange results. The discrepancy for configuration C is likely caused by the redistribution of the forearm's mass as previously described in the Power Exchange subsection. In both configurations, the compensated cases show closer agreement with the baseline configuration in which all sensors are present.

V. Conclusion

This study proposed a tuning method for removing sensors in a Kalman filter-based sensor fusion system in which any reasonable subset of sensors yields the same filter dynamics as with the full set of sensors. The dynamical impact of operating with a subset of sensors without tuning was demonstrated experimentally, which motivates the need for a systematic tuning strategy. The proposed method was verified on the EXO-UL8 exoskeleton where the output of the Kalman filter drove an admittance controller. The tuning method was applied to two different sensor configurations (configs. B and C), and retained similar performance as the original full set of sensors (config. A). Experiments performed with the EXO-UL8 quantified actual performance by calculating operator-exoskeleton power exchange and actuation stress. Results agree with theoretical expectations and support the feasibility and utility of the method.

A limitation of the method arises when sensors are located kinematically far from the joints whose torque are being estimated, such as with joint 1 in configuration B. Qualitative and quantitative assessments indicate a decrease in operator-exoskeleton transparency due to inaccuracies introduced by more intermediate joints. This limitation may be further studied by quantifying transparency as a function of sensor placement, and then implementing the optimal placement.

The proposed sensor reduction method could be applied to any physical system that implements a Kalman filter-based sensor fusion strategy, which is pervasive in the field of robotics. For future work, applying the tuning method to other robotic devices and systems using heterogeneous sensors would broaden the utility of the method. Specifically in the context of the EXO-UL8, further work may be done to explore sensor reduction in bimanual operation, or comparison to other force sensing strategies in the literature.

References

[1] Y. Shen, J. Sun, J. Ma and J. Rosen, "Admittance Control Scheme Comparison of EXO-UL8: A Dual-Arm Exoskeleton Robotic System," *IEEE 16th International Conference on Rehabilitation Robotics (ICORR)*, pp. 611–617, Jun. 2019.

[2] Y. Shen, J. Ma, B. Dobkin and J. Rosen, "Asymmetric Dual Arm Approach For Post Stroke Recovery Of Motor Functions Utilizing The EXO-UL8 Exoskeleton System: A Pilot Study," *40th Annual International Conference of the IEEE Engineering in Medicine and Biology Society (EMBC)*, pp. 1701–1707, 2019.

[3] Y. Shen, B. P. Hsiao, J. Ma and J. Rosen, "Upper limb redundancy resolution under gravitational loading conditions: Arm postural stability index based on dynamic manipulability analysis," *IEEE-RAS 17th International Conference on Humanoid Robotics (Humanoids)*, pp. 332–338, 2017.

[4] L. Xia, Y. Feng, L. Zheng, C. Wang and X. Wu, "Development of An Adaptive Iterative Learning Controller With Sensorless Force Estimator for The Hip-type Exoskeleton," *IEEE International Conference on Robotics and Biomimetics (ROBIO)*, pp. 2516–2521, 2019.

[5] B. Ugurlu, M. Nishimura, K. Hyodo, M. Kawanishi and T. Narikiyo, "A framework for sensorless torque estimation and control in wearable exoskeletons," *12th IEEE International Workshop on Advanced Motion Control (AMC)*, pp. 1–7, 2012.

[6] S. J. Ball, I. E. Brown and S. H. Scott, "MEDARM: a rehabilitation robot with 5DOF at the shoulder complex," *IEEE/ASME International Conference on Advanced Intelligent Mechatronics*, pp. 1–6, 2007.

[7] R. Richardson, M. Brown, B. Bhakta and M. C. Levesley, "Design and control of a three degree of freedom pneumatic physiotherapy robot," *Robotica*, vol. 21, no. 6, pp. 589–604, 2003.

[8] J. Fabian, Ö. Özen, P. Bösch, H. Bobrovsky, V. Klamroth-Marganska, R. Riener and G. Rauter, "Exoskeleton transparency: feed-forward compensation vs. disturbance observer," *at-Automatisierungstechnik*, vol. 66, no. 12, pp. 1014–1026, 2018.

[9] Y. Kanai and Y. Fujimoto, "Performance Analysis of Torque-sensorless Assist Control of a Powered Exoskeleton Using Highly Back-drivable Actuators," *IEEE 17th International Conference on Industrial Informatics (INDIN)*, pp. 577–582, 2019.

[10] H. Zhang, R. Ayoub and S. Sundaram, "Sensor selection for Kalman filtering of linear dynamical systems: Complexity, limitations and greedy algorithms," *Automatica*, vol. 78, pp. 202–210, Apr. 2017.

[11] S. Joshi and S. Boyd, "Sensor Selection via Convex Optimization," *IEEE Transactions on Signal Processing*, vol. 57, pp. 451-462, 2009.

[12] A. Zare, H. Mohammadi, N. K. Dhingra, T. T. Georgiou and M. R. Jovanovic, "Proximal algorithms for large-scale statistical modeling and sensor/actuator selection," *IEEE Transactions on Automatic Control*, 2019.

[13] F. Augugliaro and R. D'Andrea, "Admittance control for physical human-quadrocopter interaction," *European Control Conference (ECC)*, pp. 1805-1810, 2013.

[14] S. Nagai, R. Oboe, T. Shimono and A. Kawamura, "Fast force control without force sensor using combination of aaKF and RFOB for in-circuit test with probing system," IEEJ J. Industry Applications, vol. 8, no. 2, pp. 152–159, 2019.

[15] S. Akutsu, H. Sekiguchi, T. Nozaki and T. Murakami, "Position and torque sensorless motion transmission for haptic teleoperation using two types of voltage compensation," *24th International Conference on Mechatronics and Machine Vision in Practice*, pp. 1–6, 2017.

[16] A. Hace and M. Franc, "Pseudo-Sensorless High-Performance Bilateral Teleoperation by Sliding-Mode Control and FPGA," *IEEE/ASME Transactions on Mechatronics*, vol. 19, no. 1, pp. 384–393, Feb. 2014.

[17] D. Novak and R. Riener, "A survey of sensor fusion methods in wearable robotics," *Robotics and Autonomous Systems*, vol. 73, pp. 155–170, Nov. 2015.

[18] T. S. Li, Y. Su, S. Liu, J. Hu and C. Chen, "Dynamic Balance Control for Biped Robot Walking Using Sensor Fusion, Kalman Filter, and Fuzzy Logic," *IEEE Transactions on Industrial Electronics*, vol. 59, no. 11, pp. 4394–4408, Nov. 2012.

[19] J. L. Speyer and W. H. Chung, "Stochastic Processes, Estimation, and Control," USA, Society for Industrial and Applied Mathematics, 2008.

[20] C. Giraud and B. Jouvencel, "Sensor selection in a fusion process: a fuzzy approach," *IEEE International Conference Multisensor Fusion and Integration for Intelligent Systems*, pp. 599–606, 1994.

[21] M. Vemula and P. M. Djuric, "Multisensor fusion for target tracking using sequential monte carlo methods," *IEEE/SP 13th Workshop on Statistical Signal Processing*, pp. 1304–1309, 2005.

[22] M. Kawamura, S. Ookubo, Y. Asano, T. Kozuki, K. Okada and M. Inaba, "A joint-space controller based on redundant muscle tension for multiple DOF joints in musculoskeletal humanoids," *IEEE-RAS 16th International Conference on Humanoid Robots (Humanoids)*, pp. 814-819, 2016.

[23] Z. Xu, S. X. Yang and S. A. Gadsden, "Enhanced Bioinspired Backstepping Control for a Mobile Robot With Unscented Kalman Filter," *IEEE Access*, vol. 8, pp. 125899-125908, 2020.

[24] N. Jarrasse and G. Morel, "Connecting a Human Limb to an Exoskeleton," *IEEE Transactions on Robotics*, vol. 28, pp. 697–709, Jun. 2012.

[25] D. Simon, "Optimal State Estimation," USA, John Wiley & Sons, Inc., 2006.

[26] H. Kim, L. M. Miller, N. Byl, G. M. Abrams and J. Rosen, "Redundancy Resolution of the Human Arm and an Upper Limb Exoskeleton," *IEEE Transactions on Biomedical Engineering*, vol. 59, no. 6, pp. 1770–1779, Jun. 2012.

[27] S. G. Hart and L. E. Staveland, "Development of the NASA-TLX (Task Load Index): Results of Empirical and Theoretical Research," *Advances in Psychology*, vol. 52, pp. 139–183, 1988.

[28] P. Lee, S. Wei, J. Zhao and N. I. Badler, "Strength guided motion," *ACM SIGGRAPH Computer Graphics*, vol. 24, no. 4, pp. 253–262, 1990.